Title

Nanotopography Enhances Dynamic Remodeling of Tight Junction Proteins through Cytosolic Liquid Complexes

Journal

ACS Nano, 14(10)

ISSN

1936-0851

Authors

Huang, Xiao
Shi, Xiaoyu
Hansen, Mollie Eva
et al.

Publication Date

2020-10-27

DOI

10.1021/acsnano.0c04866

Peer reviewed

ACSNANO

www.acsnano.org

ARTICLE

Nanotopography Enhances Dynamic Remodeling of Tight Junction Proteins through Cytosolic Liquid Complexes

Xiao Huang, Xiaoyu Shi, Mollie Eva Hansen, Initha Setiady, Cameron L. Nemeth, Anna Celli, Bo Huang, Theodora Mauro, Michael Koval, and Tejal A. Desai*

Cite This: *ACS Nano* 2020, 14, 13192−13202

Read Online

ACCESS | Metrics & More | Article Recommendations | Supporting Information

ABSTRACT: **Nanotopographic materials provide special biophysical stimuli that can regulate epithelial tight junctions and their barrier function. Through the use of total internal reflection fluorescence microscopy of live cells, we demonstrated that contact of synthetic surfaces with defined nanotopography at the apical surface of epithelial monolayers increased paracellular permeability of macromolecules. To monitor changes in tight junction morphology in live cells, we fluorescently tagged the scaffold protein zonula occludens-1 (ZO-1) through CRISPR/Cas9-based gene editing to enable live cell tracking of ZO-1 expressed at physiologic levels. Contact between cells and nanostructured surfaces destabilized junction-associated ZO-1 and promoted its arrangement into highly dynamic liquid cytosolic complexes with a 1−5 μm diameter. Junction-associated ZO-1 rapidly remodeled, and we observed the direct transformation of cytosolic complexes into junction-like structures. Claudin-family tight junction transmembrane proteins and F-actin also were associated with these ZO-1 containing cytosolic complexes. These data suggest that these cytosolic structures are important intermediates formed in response to nanotopographic cues that facilitate rapid tight junction remodeling in order to regulate paracellular permeability.**

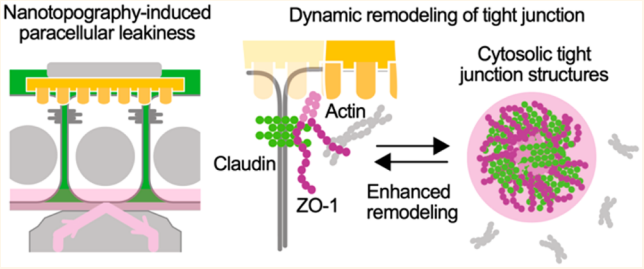

KEYWORDS: *nanotopography, tight junction, dynamic remodeling, cytosolic complex, paracellular permeability*

Tight junctions are membrane-associated protein complexes at epithelial apical intercellular contact sites, which form barriers that regulate the paracellular transit of water, ions, and molecules.[1−4] Although their barrier-forming properties and morphology suggest a static structure, in fact tight junction-associated proteins are highly dynamic and can be acutely regulated by external stimuli in a matter of minutes to hours to alter the extent of paracellular flux.[2,5] One class of stimuli are synthetic materials fabricated with specific geometries and surface topographic features at the micro- and nanoscale that have the capability to influence epithelial cell behavior.[6−8] We previously found that polymeric films with a defined nanostructure, when placed in contact with the apical surface of epithelial cells, led to enhanced transepithelial permeability of macromolecules ranging in size from ∼60 to ∼150 kDa, including bovine serum albumin and IgG.[9−11] This process is relatively rapid (within 1 h), reversible, energy-requiring, and depends on integrin binding and MLCK (myosin light chain kinase) signaling.[9,10] Immunostaining showed characteristic changes in tight junction morphology (ruffles) that were associated with increased permeability, further indicating nanotopography-induced regulation of tight junctions.[9] However, details regarding the transepithelial route and changes to tight junctions that occur in real-time in response to nanostructure contact are not yet understood and require specialized methodology. Specifically, commonly used methods used to detect epithelial paracellular flux, including transepithelial electrical resistance (TEER) and transepithelial diffusion through cell monolayers cultured on porous Transwell inserts,[12−14] measure bulk epithelial layer behavior and are unable to obtain submicrometer scale precision.[2] The established method for measuring localized permeability requires complicated chemical treatments, washing, and cell fixation.[15] Thus, an improved method with direct, live cell measurement capability is required to elucidate detailed mechanisms of transepithelial transport. To advance our

Received: June 10, 2020
Accepted: September 17, 2020
Published: September 17, 2020

https://dx.doi.org/10.1021/acsnano.0c04866
ACS Nano 2020, 14, 13192−13202

ability to analyze the effects of nanotopography on epithelial cell permeability, we developed a method using total internal reflection fluorescence (TIRF) microscopy to achieve a high-resolution visualization of the flux across a live cell layer in real-time. Human epithelial colorectal adenocarcinoma (Caco-2) cells, the most commonly used intestinal epithelial cell line model,[16,17] were cultured as a monolayer on Matrigel-coated glass chambers. TIRF microscopy specifically images the fluorescent tracker (FITC-IgG) that reaches the basal side of epithelia within ~100 nm from the glass substrate,[18] eliminating background signals from molecules that have not penetrated through the monolayer without extra washing steps (Figure 1A).

The tight junction-associated scaffold protein zonula occludens-1 (ZO-1) has been shown to be an important regulator for barrier permeability.[19−23] ZO-1 is highly mobile and readily exchanges between tight junctions and the cytosol.[2,5] This dynamic process is closely associated with binding to transmembrane tight junction proteins (e.g., claudins, JAM-A) and cytoskeletal proteins, especially actin.[19,20,22,24] Since ZO-1 has been identified as an essential mediator that senses extracellular mechanical forces,[23,25] live cell tracking of this protein and its dynamic interaction with its binding partners under nanotopographic exposure would further facilitate mechanistic investigation. However, systems incorporating fluorescently tagged proteins-of-interest for live cell imaging are frequently subject to overexpression, which can alter physiological behavior.[1,12,26] CRISPR-based site-specific engineering of endogenous ZO proteins with a fluorescent reporter provides a powerful method that enables live cell analysis of proteins expressed at physically regulated levels.[27] We tagged mCherry to ZO-1 protein under the control of its endogenous promoter in Caco-2 cell line using CRISPR-Cas9-based gene editing, enabling live cell tracking of morphological changes to ZO-1. A set of confocal fluorescence imaging parameters were optimized to compensate for the physiological but weak signal of mCherry-ZO-1. Through advanced imaging methods and fluorescence recovery after photobleaching (FRAP) assays, we identified nanostructure-induced dynamics of junction-associated ZO-1. This remodeling process was mediated through the formation of 1−5 μm liquid complexes in cytosol containing ZO-1, claudin-family transmembrane tight junction proteins, and F-actin. These ZO-1-positive cytosolic complexes are consistent with recently reported structures induced by the phase separation of ZO-1 that have been implicated as mediators for tight junction formation and mechanosensing.[25,27] Our ability to use nanotopography to stimulate active tight junction remodeling by this biophysical process provides a basis to understand mechanisms that regulate tight junction assembly and epithelial barrier function in response to the extracellular microenvironment.

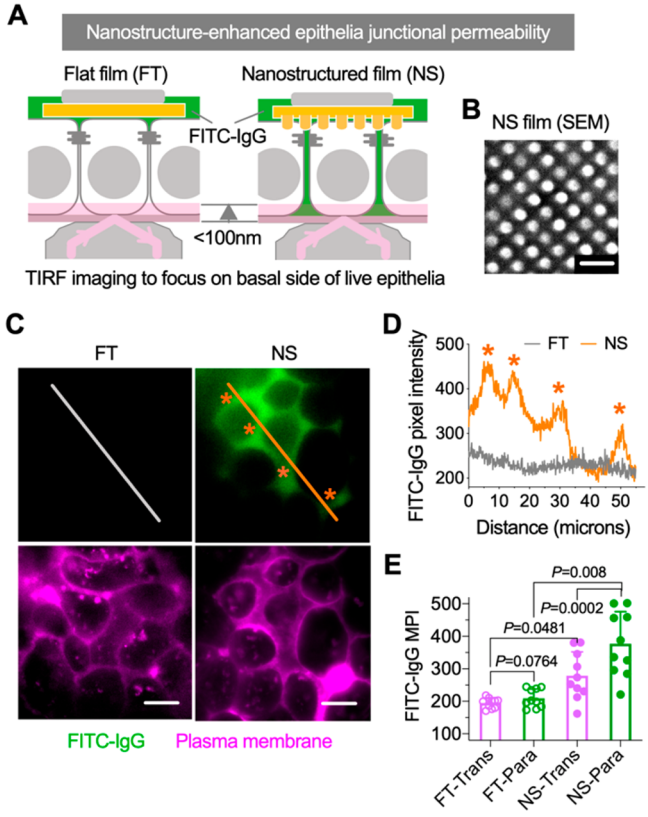

Figure 1. Enhanced paracellular permeability of Caco-2 cell monolayers induced by contact with nanotopographic surfaces. (A) Schematic of live epithelial cell basal imaging using total internal reflection fluorescence (TIRF) microscopy to track penetration of fluorescently labeled IgG. (B) Scanning electron microscopy (SEM) image of nanoimprinted polypropylene film generated from molds using electron-beam lithography. The height and width of each individual nanopillar and the space between individual nanopillars are ~200 nm. Scale bar: 400 nm. (C) TIRF images of the basal aspect of live Caco-2 monolayers treated with flat (FT) or nanostructured (NS) films together with FITC-labeled IgG molecules (green) applied to the apical side for 1 h at 37 °C (representative of n = 3 independent experiments). The pattern of FITC-IgG accumulation at the basal side of cells treated with NS films correlates with the basolateral gaps as delineated by cell membrane staining (pink), indicating paracellular permeability. Scale bar: 10 μm. (D) Transverse profile of FITC-IgG as indicated by the lines in (C), showing the accumulation of FITC-IgG at basolateral gaps due to NS film treatment. (E) The mean pixel intensity (MPI) of FITC-IgG at paracellular sites (Para) as opposed to transcellular sites (Trans) defined by plasma membrane staining in (C). Data are mean ± s.d. (n = 10 images), and the P value was determined by one-way analysis of variance (ANOVA) and Tukey's multiple comparisons test.

RESULTS AND DISCUSSION

Nanotopographic Cues Induce Paracellular Flux of Macromolecules Across Epithelial Monolayers. Caco-2 cells were cultured on Matrigel-coated glass chambers under conditions that enabled them to form a polarized monolayer (Figure 1A). Apically supplemented FITC-IgG molecules did not penetrate through the cell layer until the addition of sodium caprate, a molecule that opens tight junctions (Figure S1A).[28,29] The cells were then placed in contact with polypropylene films with or without a defined nanotopographic structure (Figure 1B). FITC-IgG was added to the apical side of the monolayer as a tracer for barrier permeability (Figure 1A, Figure S1A). We then used TIRF microscopy, which selectively illuminated fluorophores within ~100 nm zone above the glass chamber, to track the FITC-IgG penetration pattern at the basal side of the live Caco-2 monolayer with submicron resolution (Figure 1A). Acquired TIRF images were quantified using the mean FITC fluorescence intensity at the cell−cell borders marked by bulk plasma membrane with CellMask Deep Red (Figure S1B). Strikingly, FITC-IgG accumulated primarily in basolateral gaps below the cell−cell

https://dx.doi.org/10.1021/acsnano.0c04866
ACS Nano 2020, 14, 13192−13202

borders of Caco-2 monolayer after apical contact with nanostructured (NS) films for 1 h at 37 °C (Figure 1C−E, NS-Trans vs NS-Para, P = 0.0002), while FITC-IgG showed minimal paracellular permeability in flat (FT) polypropylene films treated or nontreated (NT) cells (Figure 1C−E, Figure S1C,D). NS film-treated cells showed significantly higher paracellular accumulation of FITC-IgG than cells in contact with FT films (Figure 1E, FT-Para vs NS-Para, P = 0.0080) and a higher level of transcellular accumulation (Figure 1E, NS-Trans vs FT-Trans, P = 0.0481). These data are consistent with our previous studies, which demonstrate increased transepithelial permeability to IgG when epithelial cells are in contact with nanotopographic structures, partially contributed from transcytotic transportation.[9−11] The results from TIRF microscopy confirmed paracellular permeability as a predominant route of decreased barrier function, further indicating that nanostructures regulate tight junctions.

CRISPR-Based Tagging of ZO-1 and Live Cell Imaging Reveals Cytosolic Protein Complexes Induced by Contact with Nanostructured Films. Given the important role of the ZO-1 protein in tight junction regulation,[19−23] we immunostained differentially treated cells and found a class of cytosolic complexes from the NS film treatment (Figure S1E). Considering NS-induced morphological changes in ZO-1 (Figure S1E)[9,10] and ZO-1's essential role in barrier function,[22,23] we engineered ZO-1 with a fluorescent reporter (mCherry) in Caco-2 cells to visualize the live cell response to NS treatment (Figure 2A). To maintain physiological regulation,[30] CRISPR-Cas9-based genome editing was used to precisely tag the N-terminus under the endogenous promoter (Figure 2A). The guide RNA (gRNA) was designed to target exon2 of the *TJP1* gene for site-specific insertion/deletion (indel) (Figure 2A, Figure S2A). Thereafter, the mCherry gene with two 1kb arms homologous to the indel site was integrated into the genome through homology-directed repair (HDR) (Figure 2A). Transduced Caco-2 cells were selected for mCherry-expressing cells through fluorescence-activated cell sorting (FACS) (Figure S2B), then single clones were isolated and confirmed through genomic PCR (Figure S2C). The 19 clones we isolated were all heterozygous with only one allele modified (Figure 2B, Figure S2C). Isolated clones cultured on Transwells were used for phenotypic confirmation. On the basis of TEER analysis, clone15 had a barrier function comparable to wildtype cells (Figure S2D) and thus was used for detailed imaging analysis. Through immunostaining of ZO-1 and colocalization analysis (Figure S2E), we found an equivalent morphology (Figure 2C) and that the majority of mCherry signal (~90%) colocalized with the antibody signal (Figure 2D). This suggests that the mCherry reporter faithfully represents the regulation and function of endogenous ZO-1.

Live cells expressing mCherry-ZO-1 at physiological levels were highly susceptible to photobleaching. To minimize this effect, a spinning disk confocal microscope with a high imaging speed was used to image a controlled number of z-stacks in each time-lapse. Physical drift and vibration effects were also minimized during live cell imaging using the Nikon Perfect Focus System (PFS). Additionally, mCherry-ZO-1 fluorescence was collected at an apical 1 μm z-depth with 0.3 μm intervals and z-projected the maximum pixel intensity for each time-lapse image (Figure 3A). Interestingly, we observed the existence of relatively large cytosolic structures (~1−5 μm) containing ZO-1 at the apical side next to tight junctions when

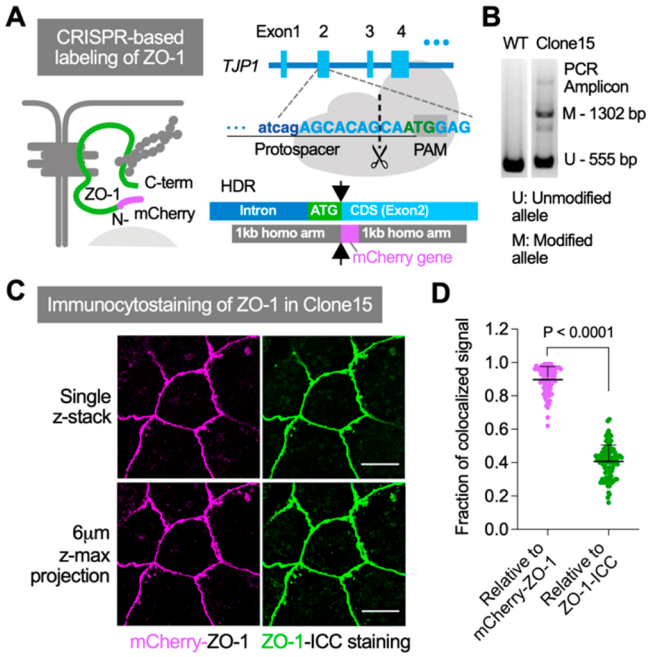

Figure 2. Tagging of endogenous ZO-1 with a mCherry reporter in Caco-2 cells through CRISPR-based genome editing and the phenotypic confirmations. (A) Schematic of CRISPR-based tagging of a mCherry reporter to the ZO-1 *N*-terminus under control of the endogenous promoter. The mCherry gene was inserted into exon2 of the *TJP1* gene through HDR. (B) Genomic PCR and agarose gel electrophoresis of a selected clone (Clone 15) detected heterozygous alleles after the insertion of the mCherry gene at the intended loci. (C) Immunocytostaining (ICC) of ZO-1 in Caco-2 Clone15 was compared to the mCherry signal to validate the fidelity of tagged-ZO-1 for live cell tracking. Images of the z-max projection were generated from the maximum pixel intensity of z-stack images acquired with 6 μm depth and 0.3 μm intervals. Scale bar: 10 μm. (D) Quantification of the fraction of the colocalized signal in (C) relative to total mCherry-ZO-1 or ZO-1-ICC signal. Data are mean ± s.d. (n = 90 images from two independent experiments), and the P value was determined by two-tailed paired t test.

cells were in contact with NS films, whereas untreated and FT film-treated cells showed fewer and smaller cytosolic ZO-1 complexes (Figure 3A). Even though cytosolic structures of ZO-1 were found in untreated cells, they were mostly located underneath the focal plane of apical tight junction structures (Figure S2F). We quantified[31] cytosolic structures in 40 μm × 40 μm apical images from five independent experiments (Figure S3A) and found a significantly higher number of large cytosolic ZO-1 complexes ($d \geq 1$ μm) in NS film-treated cells compared to untreated (P = 0.0013) or FT film-treated cells (P = 0.0090) (Figure 3B,C).

Enhanced Dynamics of Apical ZO-1 Remodeling Stimulated by Nanotopography. We then investigated the dynamics of mCherry-ZO-1 remodeling using time-lapse imaging. Strikingly, those cytosolic structures found at the apical side of nanotopography-treated cells were highly dynamic; they nucleated and coalesced with newly formed small structures (Figure 3D-i), circulated apically while collecting more ZO-1, moved toward the basal aspect of the cytoplasm (Figure 3D-ii, Movie S1), and underwent rapid reshaping, fusion and fission, exhibiting characteristics of a liquid phase as opposed to membrane vesicle-associated ZO-1

https://dx.doi.org/10.1021/acsnano.0c04866
ACS Nano 2020, 14, 13192−13202

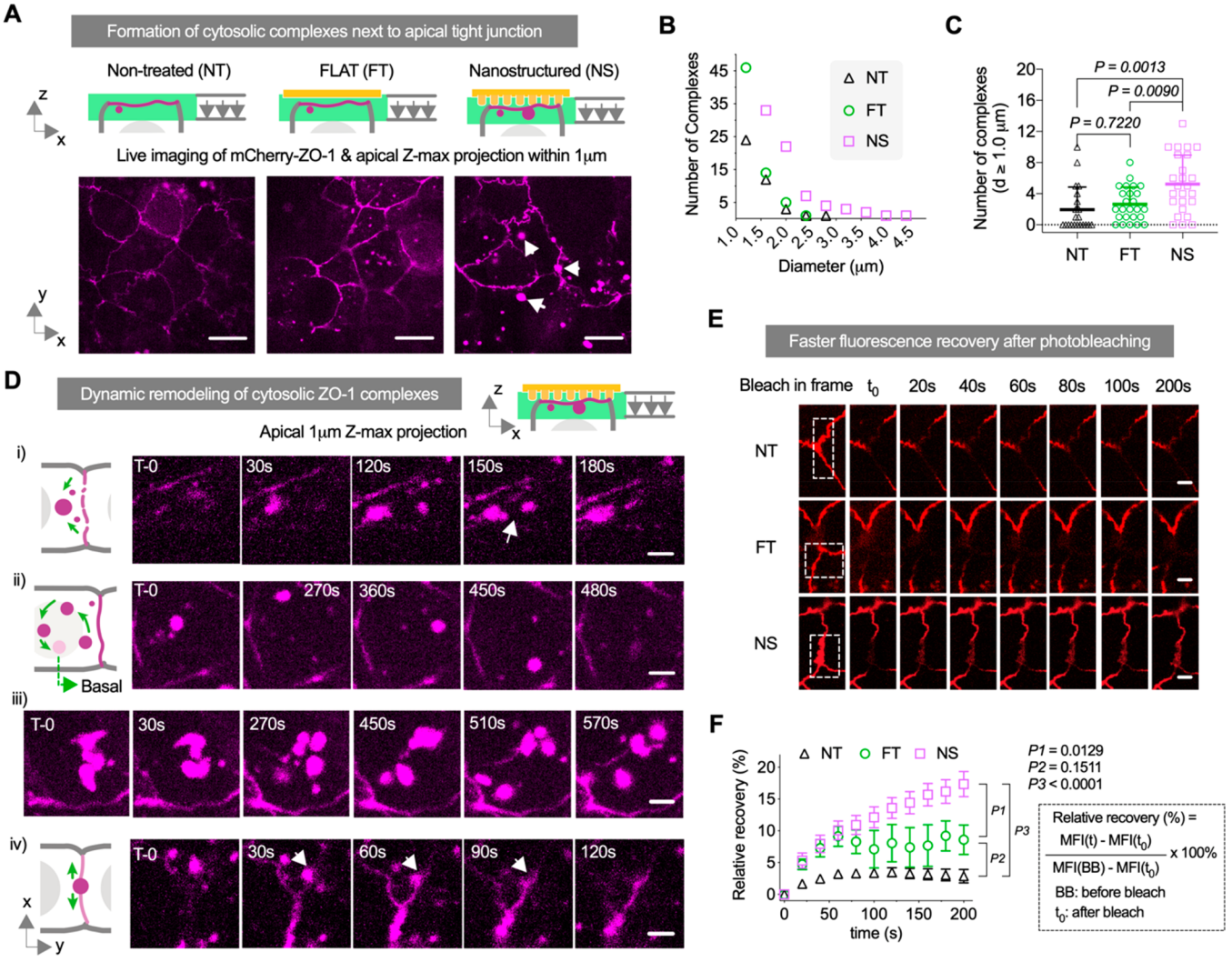

Figure 3. Enhanced dynamics of the ZO-1 protein in engineered Caco-2 cells in contact with nanostructured films. (A) Images of apical mCherry-ZO-1 (40 μm × 40 μm) in live Caco-2 monolayer cultures in contact with nanostructured (NS) or flat (FT) polypropylene films for 0.5−1.5 h at 37 °C and nontreated (NT) control. Cytosolic complexes larger than 1.0 μm diameter (white arrows) appeared at the apical side of cells in contact with an NS film. Images are projections of the maximum pixel intensity of apical z-stack images acquired with 1 μm depth and 0.3 μm intervals. Scale bar: 10 μm. (B) The size distribution of apical cytosolic complexes ($d \geq 1.0$ μm) in images represented in (A). (C) The number of ($d \geq 1.0$ μm) complexes of each image in (A). Data are mean ± s.d. (n = 25 images for each treatment from 5 independent experiments), and P values were determined by one-way ANOVA and Tukey's multiple comparisons test. (D) Time-lapse images of mCherry-tagged ZO-1 at the apical side of cells stimulated by nanotopographic cues for 0.5−1.5 h at 37 °C. The apical cytosolic ZO-1 complexes actively remodel and (i) nucleate and coalesce with newly restructured ZO-1; (ii) circulate around the cell while collecting smaller ZO-1 structures that then exit the apical focal plane; (iii) undergo reshaping, fusion, and fission; and (iv) directly transform into junction-like structures (white arrow). Images are projections of maximum pixel intensity of apical z-stack images acquired with 1 μm depth and 0.3 μm intervals. Scale bar: 2 μm. (E) Time-lapse images of junction-associated mCherry-ZO-1 after photobleaching at a selected region (white dashed line) in response to contact with either a flat (FT) or nanostructured (NS) film for 0.5−1.5 h or were nontreated (NT). Scale bar: 2 μm. (F) Quantification of relative fluorescence recovery after photobleaching (FRAP) in selected frames represented in (E). Data are mean ± s.e.m. (analyzed from 26 frames for NT, 11 frames for FT, and 29 frames for NS, pooled from 2 independent experiments), and P values were determined by one-way ANOVA analysis and Tukey's multiple comparisons test of recovery at 200 s.

(Figure 3D-iii, Movie S2). We observed two patterns of cytosolic structure nucleation: (i) the direct transition of junction-associated ZO-1 into cytosolic structures through aggregation and departure (Figure S3B-i); and (ii) the clustering of diffused signals into puncta within a network next to tight junctions (Figure S3B-ii). We also observed the direct conversion of spherical structures into linearized junction-like structures (Figure 3D-iv, Movie S2) and the rapid reorganization of ZO-1 into junction-like structures that originated from nonapical locations (Figure S3B-iii). In contrast, there were fewer and smaller ZO-1-positive cytosolic complexes in cells that were FT-treated or nontreated, and the interaction between these cytosolic structures and tight junctions was minimal (Figure S3C). With TIRF imaging at the basal side of the Caco-2 monolayer, we observed ZO-1-positive junction-like structures stimulated by apical contact with nanotopography (Figure S4A). The appearance of basal ZO-1-positive strands, together with the observation of the basal movement of cytosolic structures (Figure 3D-ii) and rapid apical junction-like structure formation (Figure S3B-iii), suggest the possible transformation of cytosolic structures to tight junction structures at basal-lateral locations. The

https://dx.doi.org/10.1021/acsnano.0c04866
ACS Nano 2020, 14, 13192−13202

formation of cytosolic ZO-1 structures was observed soon after NS film contact (~10 min, required time for treatment and live imaging setup, Figure S4B), which is consistent with the timing of TEER change from Transwell culture model in our previous studies.[9,10] FRAP bleaching of an apical cytosolic structure yielded a "half-moon" shaped structure with continuous reshaping (Figure S4C), suggesting the fast dynamics of molecular rearrangement within the structure consistent with a liquid phase.

We then used FRAP at selected regions to quantify and compare the remodeling rate of tight junctions in response to NS contact (Figure 3E). Importantly, we found that mCherry-ZO-1 fluorescence at tight junctions recovered faster after photobleaching in cells stimulated by NS films, as compared with untreated and FT film-treated cells (Figure 3F, Figure S4D,E), suggesting a higher fraction of mobile ZO-1. This further supports the finding that nanotopographic cues induce enhanced remodeling of junctional ZO-1.

Claudins Coexist in the Cytosolic Structures Stimulated by Nanotopography. To investigate the composition of cytosolic structures, we immunostained differentially treated cells for several markers, including ZO-1, claudins, F-actin, and the endocytosis marker Rab5. mCherry-positive apical cytosolic structures were confirmed to be ZO-1-positive and also colocalized with several claudins (Claudin-2, -4, -10) (Figure S5A) and F-actin (Figure S5B). Notably, the structures were negative for Rab5 staining (Figure S5B), nonacidic based on a lack of LysoTracker staining (Figure S5C), and nonmembrane-bound based on a lack of endocytosed CellMask plasma membrane label (Figure S5D), which indicates that they did not originate from vesicular mediated trafficking of endocytosed tight junction proteins.

To examine the dynamics of a transmembrane tight junction protein in live cells, we transfected mCherry-ZO-1-expressing Caco-2 cells with exogenous YFP-claudin-3 using an adenovector expression construct[32] (Figure 4A). The virus titer was optimized to minimize YFP-claudin-3 overexpression; however, this did result in heterogeneous expression by different cells in the monolayer (Figure S6). YFP-claudin-3 and mCherry-ZO-1 colocalized at apical cytosolic structures in NS film-treated cells but not in untreated or FT film-treated cells (Figure 4B,C). Importantly, claudin-3 was present in ZO-1-containing cytosolic structures at sites of formation (Figure 4D, Movie S3) and sites of interaction with tight junctions (Figure 4E). The colocalization of claudin-3, a transmembrane tight junction protein, with ZO-1, a cytosolic scaffold protein, indicates that cytosolic complexes involve the regulation of multiple classes of tight junction proteins, including transmembrane proteins.

F-Actin Engages in the Dynamics of Cytosolic Tight Junction Complexes. ZO-1 interconnects transmembrane junction proteins (e.g., claudins) and cytoskeletal F-actin in epithelial cells.[19,20] We imaged F-actin that was stained with SiR-actin in live cells under NS and FT film treatment to investigate the changes in cytoskeletal morphology in response to different stimuli (Figure 5A). We observed apparent clustering of F-actin in cells upon NS film treatment, as opposed to untreated cells or FT film treated cells. These clusters formed in response to NS contact translocated from the apical aspect of the cells to the basal side over 1.5 h (Figure S7A). More specifically, F-actin interacted with ZO-1 proteins during tight junction remodeling in several different ways (see Movie S4): (i) F-actin replaced sites of ZO-1 protein

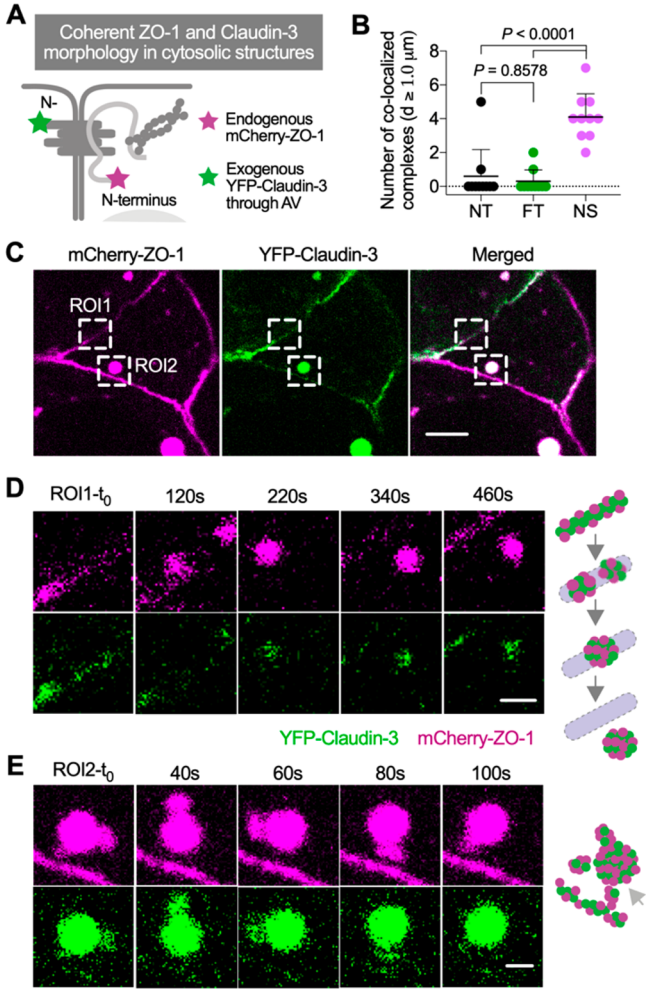

Figure 4. Apical cytosolic complexes of ZO-1 induced by nanostructures also contain claudin-family transmembrane proteins. (A) Schematic of exogenous YFP-Claudin3 adenovirus transduction in mCherry-ZO-1 engineered Caco-2 cells for live imaging analysis. Images of each time-lapse were acquired at apical 1 μm depth with 0.3 μm intervals and projected the maximum pixel intensity into presented images. (B) The number of ZO-1 and Claudin-3 colocalized complexes ($d \geq 1.0$ μm) in each 50 μm × 50 μm image of cells that were in contact with a nanostructured (NS) or flat (FT) polypropylene film for 0.5−1.5 h at 37 °C, or nontreated (NT). Data are mean ± s.d. (n = 10 images for each treatment from two independent experiments), and P values were determined by one-way ANOVA and Tukey's multiple comparisons test. (C) Images of transduced Caco-2 cells treated with a nanostructured film at 37 °C for 0.5−1.5 h, showing colocalization of ZO-1 and claudin-3 in apical cytosolic complexes. Scale bar: 10 μm. (D) Time-lapse images of ROI1 in (C) show the involvement of both ZO-1 and claudin-3 in the initiation of complex formation and cytosolic migration. (E) Time-lapse images of ROI2 in (C) show agglomeration of apical cytosolic complexes by both ZO-1 and claudin-3 next to a tight junction structure. Scale bar: 2 μm.

localization at tight junctions (Figure 5B-i); (ii) F-actin intertwined with ZO-1 in cytosolic complexes sitting next to tight junctions (Figure 5B-ii); (iii) polarized cytosolic F-actin-ZO-1 structures (Figure 5B-iii) with the F-actin portion facing toward a larger solid integrated structure as (iv) (Figure 5B-iv); and (v) F-actin and ZO-1 colocalized in large (>2 μm) hollow structures (Figure 5B-v). In some instances, F-actin/ZO-1-containing structures merged into larger colocalized

https://dx.doi.org/10.1021/acsnano.0c04866
ACS Nano 2020, 14, 13192−13202

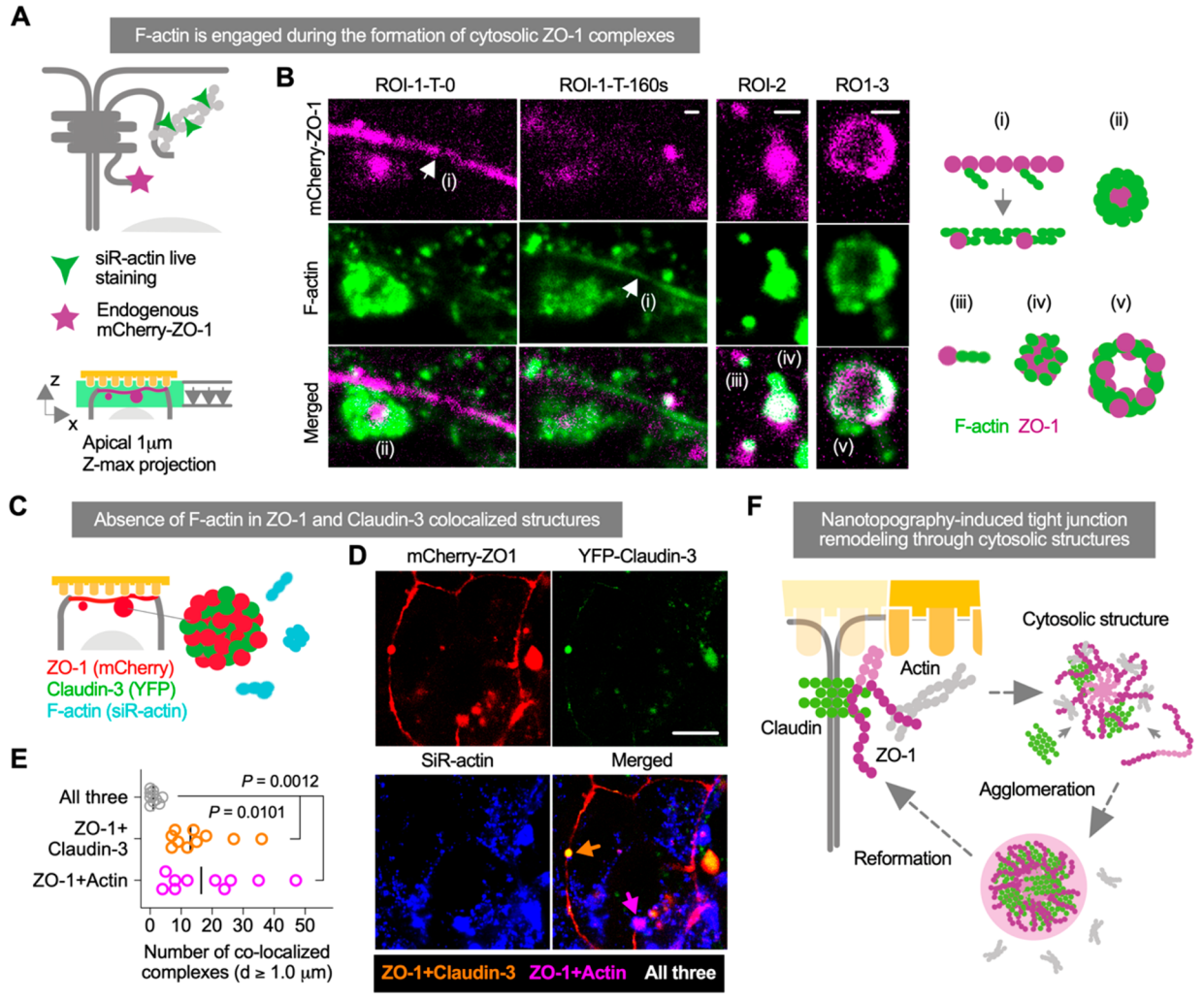

Figure 5. F-actin is engaged during the formation of cytosolic ZO-1 complexes. (A) Schematic of F-actin staining by siR-actin in mCherry-ZO-1 engineered Caco-2 cells for live imaging analysis. Images of each time-lapse are acquired at apical 1 μm depth with 0.3 μm intervals and projected the maximum pixel intensity into presented images. (B) Images of cells stimulated by nanotopographic cues for 0.5−1.5 h at 37 °C show different patterns of F-actin/ZO-1 interactions: (i) the replacement of ZO-1 with F-actin at a tight junction; (ii) F-actin wrapping around ZO-1 in a cytosolic complex next to a tight junction; (iii) a polarized cytosolic F-actin-ZO-1 complex with F-actin facing toward a larger solid integrated structure as (iv); and (v) the organization of F-actin and ZO-1 into large (>2 μm diameter) hollow structures. Scale bar: 2 μm. (C) Schematic of mCherry-ZO-1, YFP-claudin-3, and F-actin interactions in engineered Caco-2 cells for live imaging analysis. (D) Images of live cells that were stimulated by nanotopographic cues for 0.5 h at 37 °C show colocalization of ZO-1 and Claudin-3 (yellow), or ZO-1 and actin (magenta), but not all three. Scale bar: 10 μm. (E) The number of colocalized complexes ($d \geq 1.0$ μm) in 132 μm × 132 μm images represented in (D). Data were analyzed from $n = 10$ images, and P values were determined by one-way ANOVA and Tukey's multiple comparisons test. (F) Schematic overview of tight junction remodeling in response to nanotopographic cues involving ZO-1 cytosolic complexes.

structures (Figure S7B). Furthermore, there were instances where F-actin dissociated from ZO-1-containing cytosolic structures (Figure S7C,D). Similarly, cytosolic structures containing both ZO-1 and Claudin-3 lacked F-actin (Figure 5C-E), indicating that interactions of F-actin with cytosolic complexes are transient and F-actin dissociates as the complexes mature.

Through fixed staining of F-actin and its integrin adaptor protein talin,[33,34] we found that they are significantly enriched in Caco-2 cells at the apical side (~1.2 μm depth) when in contact with NS films, compared to cells treated with FT films or nontreated cells (Figure S8). This suggests that nanotopographic cues are likely to induce signaling to the cytoskeleton through apical receptors associated with integrins. Overall, our data suggest that NS materials in direct contact with the apical surface of epithelial cells enhance the dynamic remodeling of tight junctions that leads to paracellular leakiness. F-actin, a cytoskeleton protein, responds acutely to NS stimuli with rearrangements. The rearrangements are coordinated with changes in localization and morphologies of its binding partner, ZO-1. During the transition of junction-associated ZO-1 into large cytosolic complexes, transmembrane Claudin-family proteins are recruited, suggesting an unreported mechanism of tight junction regulation by biophysical stimuli (Figure. 5F).

Tight junctions, comprised of heavily cross-linked complexes of transmembrane and membrane-associated proteins, represent a structural determinant of epithelial cell polarity and regulate solute paracellular permeability.[1,3] Tight junctions are highly dynamic, even in unstimulated cells, and are acutely

https://dx.doi.org/10.1021/acsnano.0c04866
ACS Nano 2020, 14, 13192−13202

regulated by multiple extracellular biological stimuli, including hormones and cytokines.[2,5] We previously found *in vitro* and *in vivo* that cell contact with polymeric films with defined nanotopographic features enhances transepithelial permeability to macromolecules in the size range of (60−150 kDa).[9−11] Here, we utilized TIRF microscopy to directly visualize paracellular flux of FITC-IgG with submicron resolution at the basal aspect of live epithelia. The commonly used cell line Caco-2 for *in vitro* modeling of intestinal drug absorption[16,17] was cultured on Matrigel-coated glass at optimal conditions to form a polarized monolayer that blocks apically supplemented FITC-IgG. The ability to image transepithelial flux in live cell monolayers stimulated with a nanostructured biophysical cue on the apical surface provided more detailed morphological information than methods measuring bulk solute flow. Although our earlier work demonstrated that nanotopography stimulates transcytotic transportation of IgG,[11] this method enabled us to demonstrate that the paracellular route is a predominant pathway for nanostructure-induced transepithelial permeability.

ZO-1 has been shown to play an essential role in the maintenance and regulation of tight junction permeability.[22,23,25] To track the intracellular distribution of ZO-1 in live cells, we used CRISPR-Cas9-based gene editing to attach a fluorescent mCherry reporter to the N-terminus of endogenous ZO-1. Engineered ZO-1 expression was driven by its endogenous promoter, which ensured that it was expressed and regulated at physiologically relevant concentrations while simultaneously free of pitfalls related to overexpression.[1,27] Live imaging and FRAP analysis of cells triggered by nanostructured films revealed a change in the kinetics of ZO-1 turnover associated with the response of tight junctions to the contact between cells and NS films. This corresponds to our previous report[9] of NS film-induced ruffle and spike morphology of ZO-1 (Figure S1E) as a reflection of the enhanced remodeling.[35] Furthermore, the imaging methods used here also enabled us to identify an intermediate involved in nanostructure-induced remodeling of tight junctions: microscale (∼1−5 μm diameter), cytosolic ZO-1-containing complexes that colocalize with claudin-family proteins and, in some cases, F-actin. Live cell imaging analysis revealed that these nonmembrane-bound complexes (Figure S5D) have all the key signatures of a liquid state: they nucleate into spheres, they undergo reshaping, fusion, and fission, and they rearrange their contents rapidly (Figure 3D and Figure S4C).[36] This liquid cytosolic structure has the characteristics of a recently reported complex that forms as a result of the liquid−liquid phase separation of ZO-1.[27] Phase separation of ZO-1 and its accompanied junctional proteins were also reported as an important intermediate for tight junction assembly[27] and mechanosensing.[25] Here we extend these observations by showing that a nanostructured surface with the capacity to increase transepithelial permeability also induces the formation of ZO-1-positive cytosolic complexes in conjunction with an increase in tight junction remodeling. In addition, previous studies demonstrated the formation of liquid−liquid phase separated ZO-1 complexes in cell-free systems and cells overexpressing ZO-1.[27] Critically, the engineered cells we examined expressed comparable, physiologic levels of mCherry-ZO-1 as untagged ZO-1, thus demonstrating that the formation of these complexes can occur in response to a physiologic stimulus and was not driven by protein overexpression.

ZO-1 is a peripheral tight junction protein that interconnects transmembrane tight junction proteins (e.g., claudins, occludin, JAM) and F-actin.[19,20] On the basis of structure−function analysis, ZO-1 phase separation was attributed to the release of the PDZ-SH3-GuK domain that is otherwise bound by an intrinsically disordered C-terminus, and the dynamics of F-actin cytoskeleton rearrangement that can provide the tension for the release.[21,23,27] Moreover, it has been previously shown that ZO-1-positive cytosolic complexes are associated with the actin cytoskeleton that facilitated their delivery to nascent tight junctions in response to changes in tension that occur during gastrulation.[25] Similarly, we also observed that F-actin enriched and clustered at the apical side and transiently interacted with cytosolic structures in response to nanotopography. Physical cues playing a role in the formation of ZO-1 cytosolic complexes is also suggested by the apical enrichment of talin, the scaffold protein that interconnects integrin and F-actin,[33,34] and that integrin engagement and myosin activation are required for nanotopography-induced epithelial permeability.[9,10] Thus, a signal transduction pathway from membrane receptors to F-actin, ZO-1, and then to other junctional proteins may transduce physical signals from cell apical contacts to modulate tight junction function. Our *in situ* approach validates recent work demonstrating that ZO-1 phase separation mediates mechano-sensing of tight junctions.[25]

In this work, we found that nanotopographic cues under physiological conditions induced the formation of cytosolic liquid complexes containing ZO-1, tight junction proteins and actin. Liquid−liquid phase separation provides an additional mechanistic component in tight junction regulation that may be leveraged for treatment of diseases associated with barrier dysfunction.[37] Conversely, the acute modulation of tight junctions by nanotopography provides a basis for the design of *in vivo* drug delivery routes where epithelial barriers need to be circumvented, such as, oral and dermal delivery. At these interfaces, the combination of physical cues with biochemical agents may be necessary to overcome barriers such as the mucus or stratum corneum.[10] Additionally, identifying specific biological stimuli that can induce tight junction remodeling could lead to functionalized particulate nanomedicines that behave comparable to nanostructured surfaces. Such functionalized nanoparticles would have the potential to be used in intravenous applications where therapeutics often need to penetrate tissue barriers.[38−41]

CONCLUSIONS

In summary, we have developed a series of advanced imaging methods that enable the visualization of transepithelial penetration at submicron resolution and the analysis of tight junction protein dynamics in live cells. Using these approaches, we found that there were hallmark changes in ZO-1 trafficking that were associated with increased paracellular permeability of macromolecules induced by nanotopographic cues. Of particular interest, our data demonstrate that ZO-1 containing liquid cytosolic complexes can be induced to interact with tight junctions to facilitate rapid remodeling, and cytoskeleton protein F-actin was transiently involved in these complexes. This can provide a mechanistic basis for the design of drug delivery strategies dependent on precise modulation of epithelial barrier function. In addition, the imaging techniques shown here have general applicability to understanding the mechanistic basis for tight junction permeability and how

https://dx.doi.org/10.1021/acsnano.0c04866
ACS Nano 2020, 14, 13192−13202

barrier function can be modulated by other stimuli in real-time at the level of individual intercellular junctions.

MATERIALS AND METHODS

Cell Lines and Culture. The Caco-2 human colon epithelial cell line was purchased from ATCC (#HTB-37). Unless specified, cells were cultured in DMEM (Sigma, #D5796) supplemented with 20% FBS (Gemini Bio #100-106), 100 mM sodium pyruvate (Sigma #113-24-6), and penicillin−streptomycin (Sigma #516106) incubated in 5% CO_2 at 37 °C. The cells were subcultured at 90% confluency by trypsinization with 0.25% trypsin-EDTA (SM-2003). For trans-epithelial electrical resistance (TEER) measurements, cells were seeded in 6.4 mm Transwell inserts (Corning #353495) with 300 μL medium containing 84 000 cells/cm^2 seeded in the upper chamber and 500 μL medium in the bottom chamber. The medium was replenished every other day, and TEER was measured using a voltohmmeter (World Precision Instruments) from day 6 to day 16 where the measured resistance in ohms was multiplied by the area of the Transwell filter (0.3 cm^2). For live cell imaging, 200 000 cells were seeded on a 35 mm glass-bottom dish with 14 mm microwell #0 cover glass (Cellvis #D35-14-0-N), which was precoated with 0.3 mg/mL Matrigel (Corning #354234) at 37 °C for 30 min. The cell culture medium was replenished every other day. After 8−10 days, the monolayer was exchanged with cell imaging medium containing FluoroBrite DMEM Media (Thermo #A1896701) and 20% FBS for live cell imaging analysis.

CRISPR/Cas9 Knock-in in Caco-2 Cells. To generate an N-terminal mCherry knock-in in the initial exon of ZO-1, guide RNA (gRNA) for CRISPR/Cas9 mediated site-specific gene editing was designed using a Benchling CRISPR tool (www.benchling.com). gRNA targeting *TJP1* gene exon number 2−5′CCTTTATCAGAGC-ACAGCAA3′ was synthesized and complexed with trans-activating crRNA by IDT. A total of 500 000 Caco-2 cells were suspended in 100 μL of buffer (Lonza #VCA-1002) supplemented with 264 pmol of the gRNA duplex, 10 μg of the Cas9 expression plasmid (GE Healthcare #U-005100-120), and 10 μg of the repair plasmid (Genscript, Supporting Information Note S1), followed by electro-poration using program B024 of Nucleofector 2b Device (Lonza #AAB-1001). Cells were then plated in one well within a 24-well plate and supplemented with 1 mL of medium. To validate CRISPR/Cas9- and gRNA-mediated site-specific insertion/deletion (indel), cells from the transfection without the repair plasmid were collected after 3 days for genome extraction (Bioline #BIO-52066) and PCR (NEB #M0491S) at the region of the indel (forward primer, 5′TGTTTG-TGACGTTAAAGCAGCC3′; reverse primer, 5′CACAAACTTACC-CTGTGAAGCG3′). The genome indel was assessed by T7 Endonuclease I assay (NEB #M0302) followed by SDS-PAGE gel electrophoresis (Genscript #M42012L). Seven days after the transfection of the complex including the repair plasmid, cells were collected and sorted by FACS (Sony SH800) for the enrichment of mCherry-positive cells. Enriched cells were plated and subcultured in 10 cm dishes at 3000 cells per dish to produce single-cell clones. Nineteen clones were isolated after 2 weeks, further expanded, then confirmed for mCherry knock-in through genome extraction and PCR (using the same primer pair as above) and analyzed by agarose gel electrophoresis.

Nanostructured Film Fabrication and Cell Treatment. Nanostructured films were made, as previously described,[9−11] by nanoimprint lithography in which polypropylene was heated above its glass transition temperature and pressed into a silicon mold. Molds were fabricated using electron beam lithography followed by anisotropic reactive ion etching to generate precise submicron structures. Nanostructured films were characterized using a Phenom scanning electron microscope (SEM). Nanostructured films or flat (unstructured) films (outside of the imprinted region) were biopsy punched into 6 mm diameter circles with the backside of which glued to a polyethylene terephthalate film with a 0.3 inch pipet tip attached. This device attached with two metal rings (~0.2 g) was placed in direct contact with a cell monolayer on the apical side and used for cell studies.

TIRF Microscopy for Paracellular Flux Analysis. Caco-2 cell monolayers, cultured on glass-bottom tissue culture dishes, were stained for plasma membranes (CellMask Deep Red Stain, 5 μg/mL, Thermo #C10046) and nuclei (Hoechst 33342, 5 μg/mL, Thermo #H3570) at 37 °C for 10 min in DMEM medium without FBS, then rinsed twice using cell imaging medium. A NS (nanostructured) or FT (flat) film device was placed in contact with cells on the apical side, and FITC-IgG (Sigma #F9636) was supplemented to the cell imaging medium at 10 μg/mL. After incubation at 37 °C for 1 h, live cells were imaged using an OMX-SR microscope (GE Health Care) in the ring-TIRF mode equipped with PCO Edge 5.5 cMOS cameras, 4-line laser launch 405/488/568/60 nm (Toptica), and live cell chamber at 37° with 5% CO_2. Images were acquired using a Plan ApoN 60x/1.42 (Olympus) oil immersion objective with laser liquid 1.518 (Cargile) and filter sets for DAPI (435/31), GFP (528/48), mCherry (609/37) and Cy5 (683/40). Registration alignment was determined using an image registration target slide (GE Health Care, pat #52-852833-000) and processed with SoftWoRx 7.0.0. software (GE Health Care). To quantify the paracellular permeability of FITC-IgG, the cell−cell border area in each image was outlined by a mask in the Fiji software that was generated using signals from the plasma membrane stain. The mean pixel intensity of the FITC signal was analyzed within the mask-identified area.

Confocal Microscopy of Live Caco-2 Cells. Caco-2 cells were fluorescently labeled for different proteins and cell machineries as specified before live cell film device treatment and imaging. For fluorescence tagging of claudin-3, adenovirus-carrying YFP-claudin-3 genes were prepared as described[32] and added to Caco-2 cells at ~100 MOI (multiplicity of infection) 2 days prior to imaging. Adenovirus-containing medium was removed by a fresh medium exchange 1 day after infection. For F-actin staining, SiR-actin (Cytoskeleton, #CY-SC001) was added into the medium at 0.2 μM the day before imaging, and the medium was replenished with the imaging medium right before imaging. For lysosome staining, LysoTracker Blue (Invitrogen #L7525) was added to the cell culture medium at 60 nM and incubated for 1 h at 37 °C, and then the imaging medium was replenished prior to imaging. For plasma membrane staining, CellMask Plasma Membrane Stains (ThermoFisher #C10046) was added to the FluoroBrite DMEM Media at 5 μg/mL and incubated for 10 min at 37 °C, followed by three rinses. Live cell images were acquired within 90 min after the treatment of film device on a spinning disk confocal microscope (Nikon Ti inverted microscope with Andor Borealis CSU-W1 spinning disk and Andor Zyla 4.2 sCMOS camera) equipped with a Plan Apo VC 100x/1.4 (Olympus) oil immersion objective, 4-line laser launch 405/488/561/640 nm (Andor), and live cell chamber at 37° with 5% CO_2. The microscope was controlled using a micromanager, and the Nikon Perfect Focus System was used to adjust for axial focus fluctuations.

Fluorescence Recovery after Photobleaching (FRAP). FRAP experiments in cells were carried out using the Nikon spinning disk confocal microscope described above with the following settings. Each region of interest (ROI) (less than 10 μm × 10 μm) was bleached using a 473 nm diode with 30 mW at the back focal plane of the objective with 10 repeats. Several junctions within the field of view were bleached but at a density of only one junction per cell. Prebleach and postbleach images were acquired with a 561 nm laser with 30 mW and 300 ms exposure. Fluorescence recovery of mCherry was monitored for 200 s with a time resolution of 20 s. The mean fluorescence intensity (MFI) of the bleached area was quantified using the Fiji software, and cell movements during the recovery were corrected by manual adjustment. Image groups were blinded for the analyzer during the quantification. Relative FRAP efficiency was calculated using the following formula (t, time point; BB, before bleach; t_0, 0 s after bleach) and compared among different treatment groups: NT (nontreated), FT (flat), and NS (nanostructured)

$$\%\text{Recovery} = \frac{\text{MFI(t)} - \text{MFI(t}^0\text{)}}{\text{MFI(BB)} - \text{MFI(t}^0\text{)}} \times 100$$

https://dx.doi.org/10.1021/acsnano.0c04866
ACS Nano 2020, 14, 13192−13202

Quantification of Cytosolic Complexes. In each image, a 40 μm × 40 μm frame that covers the cell's apical side with tight junctions was selected, and the cytosolic ZO-1 complexes were quantified using ImageJ with the following steps.[31] A median-blur filter was first applied to the image to reduce noise. Then, cytosolic structures were segmented using the interactive h-maxima watershed tool, where parameters including seed dynamics, intensity threshold, and peak flooding were optimized and kept constant for images across treatments within the same independent experiment. The binary image generated from the watershed results included the majority of cytosolic structures and a portion of the tight junctions as well. Afterward, the particle analysis function was used to isolate spherical cytosolic structures and report size distribution. Image groups were blinded for the analyzer during the quantification.

Cell Fixation and Staining. Caco-2 cells on tissue culture dishes were rinsed with PBS (with Ca^{2+} and Mg^{2+}) three times and fixed at room temperature in 2% paraformaldehyde/PBS (Electron Microscopy Sciences #RT-15710) for 15 min. Cells were then washed once with PBS, and residual paraformaldehyde was quenched using 1 M glycine (Sigma #50046) in PBS for 10 min. Each of the following wash steps was carried out at room temperature for 5 min. After three washes using PBS, cells were further fixed/permeabilized using methanol/acetone solution (v/v: 50/50) for exactly 2 min at room temperature. Cells were then sequentially washed three times with PBS, once with 0.5% TritonX-100 in PBS then twice with 2% goat serum (Sigma #G9023) and 0.5% TritonX-100 in PBS. Primary antibodies including anti-ZO-1 (Thermo #339188), anti-Claudin-2 (#ab53032), anti-Claudin-4 (Abcam #53156), anti-Claudin-10 (Thermo #38−8400), anti-Rab5 (Abcam #ab18211), and anti-Talin (Proteintech #14168−1-AP) were used for specific immunostaining. Cells were stained for 1 h at room temperature in PBS supplemented with 2% goat serum and antibody, then washed three times with PBS with 2% goat serum. Cells were then stained with secondary antibodies, including goat antimouse-Alexa Fluor 488 (Thermo #A11029) and goat antirabbit-Alexa Fluor 633 (Thermo #A21070), in PBS with 2% goat serum at room temperature for 1 h. For F-actin staining after fixation, Alexa Fluor 488 Phalloidin was added into the secondary antibody staining mixture. Cells were washed three times with PBS then imaged using the spinning disk confocal microscope described above.

Quantification of Colocalization. For the quantification of colocalization between mCherry-ZO-1 and immunostained ZO-1 in CRISPR-engineered cells, images acquired by the spinning disk confocal fluorescence microscope were analyzed in the CellProfiler software. In each image pair, signals from mCherry-ZO-1 and immunostained ZO-1 were identified as separate primary objects through arbitrarily determined segmentation, where an Otsu three-class thresholding method was utilized and parameters, including the object diameter and threshold correction factor, were optimized and kept constant for all images within the same experiment. The relationship between the segmented objects were defined as colocalized or noncolocalized. The fraction of colocalized signal relative to the total signal of each object (mCherry-ZO-1 or immunostained ZO-1) was determined individually.

For the quantification of cytosolic structures ($d \geq 1.0$ μm) that contained two or three colocalized signals (e.g., mCherry-ZO-1, YFP-Claudin-3, siR-actin), images from individual channels were processed in ImageJ software with "AND" calculation to yield colocalized images. These images were then segmented in the CellProfiler software using the Otsu three-class thresholding method with constant adjustment parameters within the same experiment. Spherical structures ($d \geq 1.0$ μm) were then isolated, and the size distribution of the structures was exported.

Statistical Analysis. Unless specified, all data are expressed as the mean ± the standard deviation (SD). The value of n and what n represents (e.g., number of images, experimental replicates, or independent experiments) is stated in the figure legends and the results. Statistical analysis was performed in Prism 8 (GraphPad Inc.), and the statistical test used is indicated in the relevant figure legend.

ASSOCIATED CONTENT

Supporting Information

The Supporting Information is available free of charge at https://pubs.acs.org/doi/10.1021/acsnano.0c04866.

Supplementary Figures S1−S8 including TIRF-based transepithelial flux controls; CRISPR-based tagging of ZO-1; ZO-1 live imaging and FRAP controls; compositional identification of cytosolic structures by live or dead cell staining; and F-actin-ZO-1 dynamics (PDF)

Time-lapse movie of mCherry-tagged ZO-1 at the apical side of Caco-2 cells stimulated by nanotopographic cues, showing apical cytosolic complex circulates while collecting smaller ZO-1 structures which then moves basolaterally. This movie represents images in Figure 3D-ii (AVI)

Time-lapse movie of mCherry-tagged ZO-1 at the apical side of Caco-2 cells stimulated by nanotopographic cues, showing active remodeling of cytosolic complexes and their interaction with junction-associated structures. This movie represents images in Figure 3D-iii (AVI)

Time-lapse movie of mCherry-tagged ZO-1 (purple) and YFP-tagged claudin-3 (green) at the apical side of Caco-2 cells stimulated by nanotopographic cues, showing the involvement of both proteins in the initiation of complex formation and cytosolic migration. This movie represents images in Figure 4D (AVI)

Time-lapse movie of mCherry-tagged ZO-1 (purple) and live-stained F-actin (green) at the apical side of Caco-2 cells stimulated by nanotopographic cues, showing (i) disappearance of ZO-1 concomitant with the appearance of F-actin; (ii) F-actin wrapped around ZO-1 in cytosolic complex next to a tight junction; and (iii) a large ZO-1 cytosolic complex lack of F-actin. This movie represents images in Figure 5B,D (AVI)

AUTHOR INFORMATION

Corresponding Author

Tejal A. Desai − *Department of Bioengineering and Therapeutic Sciences and UC Berkeley-UCSF Graduate Program in Bioengineering, University of California, San Francisco, San Francisco, California 94158, United States*; Email: tejal.desai@ucsf.edu

Authors

Xiao Huang − *Department of Bioengineering and Therapeutic Sciences, University of California, San Francisco, San Francisco, California 94158, United States*

Xiaoyu Shi − *Department of Pharmaceutical Chemistry, University of California, San Francisco, San Francisco, California 94158, United States; Department of Developmental and Cell Biology, University of California, Irvine, Irvine, California 92697, United States*

Mollie Eva Hansen − *UC Berkeley-UCSF Graduate Program in Bioengineering, University of California, San Francisco, San Francisco, California 94158, United States*

Initha Setiady − *Department of Bioengineering and Therapeutic Sciences, University of California, San Francisco, San Francisco, California 94158, United States*

Cameron L. Nemeth − *UC Berkeley-UCSF Graduate Program in Bioengineering, University of California, San Francisco, San Francisco, California 94158, United States*

https://dx.doi.org/10.1021/acsnano.0c04866
ACS Nano 2020, 14, 13192−13202

Anna Celli − *Department of Dermatology, University of California, San Francisco, San Francisco, California 94158, United States*

Bo Huang − *Department of Pharmaceutical Chemistry and Department of Biochemistry and Biophysics, University of California, San Francisco, San Francisco, California 94158, United States; Chan Zuckerberg Biohub, San Francisco, California 94158, United States;* orcid.org/0000-0003-1704-4141

Theodora Mauro − *Department of Dermatology, University of California, San Francisco, San Francisco, California 94158, United States*

Michael Koval − *Division of Pulmonary, Allergy, and Critical Care Medicine and Department of Cell Biology, Emory University School of Medicine, Atlanta, Georgia 30322, United States*

Complete contact information is available at: https://pubs.acs.org/10.1021/acsnano.0c04866

Author Contributions

X.H., X.S., M.K., and T.A.D designed the research. X.H. carried out the experiments. X.H., M.E.H, and I.S. analyzed the data. X.H., X.S., A.C., T.M., M.K., and T.A.D interpreted the results. X.H. drafted the manuscript. X.H., M.K., X.S., C.N., B.H., T.M., and T.A.D. edited the manuscript.

Funding

This research was supported by the National Institutes of Health Grant 1R01EB018842 to T.A.D. and M.K. X.H. was supported by a Li foundation fellowship. X.S. was supported by the NIH Pathway to Independence Award R00GM126136. B.H. is a Chan Zuckerberg Biohub Investigator.

Notes

The authors declare no competing financial interest.
A preprint of this work has been posted.[42]

ACKNOWLEDGMENTS

We thank H. Zeng for advice on CRISPR engineering, R. Dodge for help with figure graphics, and K. Herrington for advice on cell imaging.

REFERENCES

(1) Steed, E.; Balda, M. S.; Matter, K. Dynamics and Functions of Tight Junctions. *Trends Cell Biol.* **2010**, *20*, 142−149.
(2) Shen, L.; Weber, C. R.; Raleigh, D. R.; Yu, D.; Turner, J. R. Tight Junction Pore and Leak Pathways: A Dynamic Duo. *Annu. Rev. Physiol.* **2011**, *73*, 283−309.
(3) Anderson, J. M.; Van Itallie, C. M. Physiology and Function of the Tight Junction. *Cold Spring Harb. Perspect. Biol.* **2009**, *1*, a002584.
(4) Barua, S.; Mitragotri, S. Challenges Associated with Penetration of Nanoparticles across Cell and Tissue Barriers: A Review of Current Status and Future Prospects. *Nano Today* **2014**, *9*, 223−243.
(5) Shen, L.; Weber, C. R.; Turner, J. R. The Tight Junction Protein Complex Undergoes Rapid and Continuous Molecular Remodeling at Steady State. *J. Cell Biol.* **2008**, *181*, 683−695.
(6) Fox, C. B.; Kim, J.; Le, L. V.; Nemeth, C. L.; Chirra, H. D.; Desai, T. A. Micro/Nanofabricated Platforms for Oral Drug Delivery. *J. Controlled Release* **2015**, *219*, 431−444.
(7) Le, L. V.; Mkrtschjan, M. A.; Russell, B.; Desai, T. A. Hang on Tight: Reprogramming the Cell with Microstructural Cues. *Biomed. Microdevices* **2019**, *21*, 43.
(8) Lamson, N. G.; Berger, A.; Fein, K. C.; Whitehead, K. A. Anionic Nanoparticles Enable the Oral Delivery of Proteins by Enhancing Intestinal Permeability. *Nat. Biomed. Eng.* **2020**, *4*, 84−96.
(9) Kam, K. R.; Walsh, L. A.; Bock, S. M.; Koval, M.; Fischer, K. E.; Ross, R. F.; Desai, T. A. Nanostructure-mediated Transport of Biologics across Epithelial Tissue: Enhancing Permeability *via* Nanotopography. *Nano Lett.* **2013**, *13*, 164−171.
(10) Walsh, L.; Ryu, J.; Bock, S.; Koval, M.; Mauro, T.; Ross, R.; Desai, T. Nanotopography Facilitates *in Vivo* Transdermal Delivery of High Molecular Weight Therapeutics Through an Integrin-dependent Mechanism. *Nano Lett.* **2015**, *15*, 2434−2441.
(11) Stewart, T.; Koval, W. T.; Molina, S. A.; Bock, S. M.; Lillard, J. W., Jr.; Ross, R. F.; Desai, T. A.; Koval, M. Calibrated Flux Measurements Reveal a Nanostructure-stimulated Transcytotic Pathway. *Exp. Cell Res.* **2017**, *355*, 153−161.
(12) Balda, M. S.; Whitney, J. A.; Flores, C.; Gonzalez, S.; Cereijido, M.; Matter, K. Functional Dissociation of Paracellular Permeability and Transepithelial Electrical Resistance and Disruption of the Apical-basolateral Intramembrane Diffusion Barrier by Expression of a Mutant Tight Junction Membrane Protein. *J. Cell Biol.* **1996**, *134*, 1031−1049.
(13) Srinivasan, B.; Kolli, A. R.; Esch, M. B.; Abaci, H. E.; Shuler, M. L.; Hickman, J. J. TEER Measurement Techniques for *in Vitro* Barrier Model Systems. *J. Lab. Autom.* **2015**, *20*, 107−126.
(14) Yeste, J.; Illa, X.; Alvarez, M.; Villa, R. Engineering and Monitoring Cellular Barrier Models. *J. Biol. Eng.* **2018**, *12*, 18.
(15) Dubrovskyi, O.; Birukova, A. A.; Birukov, K. G. Measurement of Local Permeability at Subcellular Level in Cell Models of Agonist- and Ventilator-induced Lung Injury. *Lab. Invest.* **2013**, *93*, 254−263.
(16) Lamson, N. G.; Ball, R. L.; Fein, K. C.; Whitehead, K. A. Thrifty, Rapid Intestinal Monolayers (TRIM) Using Caco-2 Epithelial Cells for Oral Drug Delivery Experiments. *Pharm. Res.* **2019**, *36*, 172.
(17) Artursson, P.; Palm, K.; Luthman, K. Caco-2 Monolayers in Experimental and Theoretical Predictions of Drug Transport. *Adv. Drug Delivery Rev.* **2001**, *46*, 27−43.
(18) Mattheyses, A. L.; Simon, S. M.; Rappoport, J. Z. Imaging with Total Internal Reflection Fluorescence Microscopy for the Cell Biologist. *J. Cell Sci.* **2010**, *123*, 3621−3628.
(19) Odenwald, M. A.; Choi, W.; Kuo, W. T.; Singh, G.; Sailer, A.; Wang, Y.; Shen, L.; Fanning, A. S.; Turner, J. R. The Scaffolding Protein ZO-1 Coordinates Actomyosin and Epithelial Apical Specializations *in Vitro* and *in Vivo*. *J. Biol. Chem.* **2018**, *293*, 17317−17335.
(20) Fanning, A. S.; Jameson, B. J.; Jesaitis, L. A.; Anderson, J. M. The Tight Junction Protein ZO-1 Establishes a Link between the Transmembrane Protein Occludin and the Actin Cytoskeleton. *J. Biol. Chem.* **1998**, *273*, 29745−29753.
(21) Rodgers, L. S.; Beam, M. T.; Anderson, J. M.; Fanning, A. S. Epithelial Barrier Assembly Requires Coordinated Activity of Multiple Domains of the Tight Junction Protein ZO-1. *J. Cell Sci.* **2013**, *126*, 1565−1575.
(22) Yu, D.; Marchiando, A. M.; Weber, C. R.; Raleigh, D. R.; Wang, Y.; Shen, L.; Turner, J. R. MLCK-dependent Exchange and Actin Binding Region-dependent Anchoring of ZO-1 Regulate Tight Junction Barrier Function. *Proc. Natl. Acad. Sci. U. S. A.* **2010**, *107*, 8237−8241.
(23) Spadaro, D.; Le, S.; Laroche, T.; Mean, I.; Jond, L.; Yan, J.; Citi, S. Tension-dependent Stretching Activates ZO-1 to Control the Junctional Localization of Its Interactors. *Curr. Biol.* **2017**, *27*, 3783−3795.
(24) Belardi, B.; Hamkins-Indik, T.; Harris, A. R.; Kim, J.; Xu, K.; Fletcher, D. A. A Weak Link with Actin Organizes Tight Junctions to Control Epithelial Permeability. *Dev. Cell* **2020**, in press. DOI: 10.1016/j.devcel.2020.07.022.
(25) Schwayer, C.; Shamipour, S.; Pranjic-Ferscha, K.; Schauer, A.; Balda, M.; Tada, M.; Matter, K.; Heisenberg, C. P. Mechanosensation of Tight Junctions Depends on ZO-1 Phase Separation and Flow. *Cell* **2019**, *179*, 937−952.
(26) McCarthy, K. M.; Francis, S. A.; McCormack, J. M.; Lai, J.; Rogers, R. A.; Skare, I. B.; Lynch, R. D.; Schneeberger, E. E. Inducible Expression of Claudin-1-Myc but Not Occludin-VSV-G Results in

Aberrant Tight Junction Strand Formation in MDCK Cells. *J. Cell Sci.* **2000**, *113*, 3387−3398.
(27) Beutel, O.; Maraspini, R.; Pombo-Garcia, K.; Martin-Lemaitre, C.; Honigmann, A. Phase Separation of Zonula Occludens Proteins Drives Formation of Tight Junctions. *Cell* **2019**, *179*, 923−936.
(28) Kurasawa, M.; Kuroda, S.; Kida, N.; Murata, M.; Oba, A.; Yamamoto, T.; Sasaki, H. Regulation of Tight Junction Permeability by Sodium Caprate in Human Keratinocytes and Reconstructed Epidermis. *Biochem. Biophys. Res. Commun.* **2009**, *381*, 171−175.
(29) Krug, S. M.; Amasheh, M.; Dittmann, I.; Christoffel, I.; Fromm, M.; Amasheh, S. Sodium Caprate as an Enhancer of Macromolecule Permeation across Tricellular Tight Junctions of Intestinal Cells. *Biomaterials* **2013**, *34*, 275−282.
(30) Riesen, F. K.; Rothen-Rutishauser, B.; Wunderli-Allenspach, H. A ZO1-GFP Fusion Protein to Study the Dynamics of Tight Junctions in Living Cells. *Histochem. Cell Biol.* **2002**, *117*, 307−315.
(31) Brazill, J. M.; Zhu, Y.; Li, C.; Zhai, R. G. Quantitative Cell Biology of Neurodegeneration in Drosophila through Unbiased Analysis of Fluorescently Tagged Proteins Using Imagej. *J. Visualized Exp.* **2018**, *138*, 58041.
(32) Mitchell, L. A.; Overgaard, C. E.; Ward, C.; Margulies, S. S.; Koval, M. Differential Effects of Claudin-3 and Claudin-4 on Alveolar Epithelial Barrier Function. *Am. J. Physiol.: Lung Cell. Mol. Physiol.* **2011**, *301*, L40−L49.
(33) Sun, Z.; Costell, M.; Fassler, R. Integrin Activation by Talin, Kindlin and Mechanical Forces. *Nat. Cell Biol.* **2019**, *21*, 25−31.
(34) Kalappurakkal, J. M.; Anilkumar, A. A.; Patra, C.; van Zanten, T. S.; Sheetz, M. P.; Mayor, S. Integrin Mechano-chemical Signaling Generates Plasma Membrane Nanodomains That Promote Cell Spreading. *Cell* **2019**, *177*, 1738−1756.
(35) Lynn, K. S.; Peterson, R. J.; Koval, M. Ruffles and Spikes: Control of Tight Junction Morphology and Permeability by Claudins. *Biochim. Biophys. Acta, Biomembr.* **2020**, *1862*, 183339.
(36) Hyman, A. A.; Weber, C. A.; Julicher, F. Liquid-liquid Phase Separation in Biology. *Annu. Rev. Cell Dev. Biol.* **2014**, *30*, 39−58.
(37) Sun, S.; Zhou, J. Phase Separation as a Therapeutic Target in Tight Junction-associated Human Diseases. *Acta Pharmacol. Sin.* **2020**, *0*, 1−4.
(38) Shuvaev, V. V.; Khoshnejad, M.; Pulsipher, K. W.; Kiseleva, R. Y.; Arguiri, E.; Cheung-Lau, J. C.; LeFort, K. M.; Christofidou-Solomidou, M.; Stan, R. V.; Dmochowski, I. J.; Muzykantov, V. R. Spatially Controlled Assembly of Affinity Ligand and Enzyme Cargo Enables Targeting Ferritin Nanocarriers to Caveolae. *Biomaterials* **2018**, *185*, 348−359.
(39) Myerson, J. W.; Braender, B.; McPherson, O.; Glassman, P. M.; Kiseleva, R. Y.; Shuvaev, V. V.; Marcos-Contreras, O.; Grady, M. E.; Lee, H. S.; Greineder, C. F.; Stan, R. V.; Composto, R. J.; Eckmann, D. M.; Muzykantov, V. R. Flexible Nanoparticles Reach Sterically Obscured Endothelial Targets Inaccessible to Rigid Nanoparticles. *Adv. Mater.* **2018**, *30*, No. 1802373.
(40) Uhl, C. G.; Muzykantov, V. R.; Liu, Y. Biomimetic Microfluidic Platform for the Quantification of Transient Endothelial Monolayer Permeability and Therapeutic Transport under Mimicked Cancerous Conditions. *Biomicrofluidics* **2018**, *12*, 014101.
(41) Thomas, A.; Daniel Ou-Yang, H.; Lowe-Krentz, L.; Muzykantov, V. R.; Liu, Y. Biomimetic Channel Modeling Local Vascular Dynamics of Pro-inflammatory Endothelial Changes. *Biomicrofluidics* **2016**, *10*, 014101.
(42) Huang, X.; Shi, X.; Hansen, M. E.; Nemeth, C. L.; Celli, A.; Huang, B.; Mauro, T.; Koval, M.; Desai, T. A. Nanotopography Enhances Dynamic Remodeling of Tight Junction Proteins through Cytosolic Complexes. *bioRxiv* **2019**, DOI: 10.1101/858118.

https://dx.doi.org/10.1021/acsnano.0c04866
ACS Nano 2020, 14, 13192−13202